



## OPEN

## SUBJECT AREAS:

ELECTRICAL AND  
ELECTRONIC  
ENGINEERINGELECTRONIC AND SPINTRONIC  
DEVICESEffect of Band-Alignment Operation on  
Carrier Transport in  $\text{Bi}_2\text{Se}_3$  Topological  
Insulator

Gaurav Gupta, Mansoor Bin Abdul Jalil &amp; Gengchiao Liang

Department of Electrical and Computer Engineering, National University of Singapore, Singapore 117576.

Received  
25 June 2014Accepted  
11 August 2014Published  
28 August 2014

Correspondence and  
requests for materials  
should be addressed to  
G.G. (a0089293@  
nus.edu.sg) or G.L.  
(elelg@nus.edu.sg)

Band-alignment induced current modulation in  $\text{Bi}_2\text{Se}_3$  three-dimensional topological insulator slab has been investigated by quantum transport simulations for three different device designs, one for purely lateral transport and other two with vertical transport. Non-Equilibrium Green Function formalism has been deployed to understand the transport mechanism in band-alignment devices to appraise the possibility of a 3D-TI based resonant device. A resonance condition is observed when the Dirac-points (bands) are aligned. This results in the maximum current at resonance for the design with only lateral transport. However, current ratio between resonant and non-resonant condition is found to be relatively small and strong temperature dependence is also noticed. The other two designs with vertical transport have degraded transfer characteristics, although from state-of-art literature they are expected to manifest nearly an ideal resonance peak. The physical insights for these observations have been posited along with the suggestions for attaining close to an ideal operation for the first design, which we also suggest for the pursuit in the future for spintronic oscillators and analog multipliers based on band-alignment induced resonance.

Graphene-like gapless linear Dirac-bands, but in odd numbers, on the surface of three-dimensional (3D)<sup>1</sup> topological insulators (TI), with bulk insulating phase, have excellent transport properties. Time-reversal symmetry protects these surface states against any non-magnetic perturbation<sup>2</sup> to ensure high conductivity by suppressing backscattering, which makes 3D-TI suitable for applications like interconnects<sup>3</sup> and quantum computing<sup>4</sup>. Furthermore, spin-momentum locking<sup>5</sup> for carrier transport in these helical surface states projects TI also as a promising candidate for spintronic applications<sup>6,7</sup>, which gives it an advantage over spin-degenerate dual-valley graphene Dirac-bands. Among the extant 3D-TI,  $\text{Bi}_2\text{Se}_3$ <sup>8</sup> has the largest bulk bandgap of 0.3 eV<sup>9</sup> which provides large energy window for exploiting these exotic surface states in TI, and hence has been chosen as representative material in this work. Recently, there has been a surge in device proposals<sup>10–12</sup> to regulate electron flow in Dirac-band materials via band-modulation by filtering out unwanted momentum states. Furthermore, by leveraging on the Dirac-bands of graphene, recently there has been a proposal of the symmetric Field Effect Transistor (SymFET)<sup>13</sup>, a novel device with a resonant current peak for an appropriate balance of channel bias ( $V_{\text{DS}}$ ) with Fermi-level ( $E_F$ ). This device based on vertical tunneling from n-doped layer to p-doped layer, separated by an insulator, is expected to exhibit a large current switching ratio which is symmetrical about resonance peak, at which the Dirac-points (bands) exactly align between two layers (see Fig. 4(b) of Ref. 13). The device operation has also been shown analytically<sup>13</sup> to be robust against temperature variation. Consequently, this device has been considered as a good candidate for designing high-speed analog multipliers and oscillators<sup>13</sup>. Such high-speed multipliers and oscillators in spintronic circuits would serve an important role in hybrid logic based systems<sup>14</sup> with 3D-TI serving a common platform for components.

In this work, therefore, we comprehensively investigate the transport mechanism in band-alignment devices to appraise the possibility of a similar resonance state in 3D-TI which may serve as an analogue of multipliers and oscillators in the spintronic circuits. For this purpose three different device designs are evaluated, one purely for lateral transport (Design-A) and two for vertical transport (Design-B and Design-C), to operate in the helical surface bands. Design-A presents a simple understanding of band-alignment concept and explains the effect of mode-matching (electron momentum modes), gate-tunable density of states (DOS) and temperature on transfer characteristics of the device. Design-B emulates the symFET concept in 3D-TI to peruse its assumptions via quantum transport investigation. Although a similar resonant state is observed, its effectiveness is much weaker than originally expected for which reasons have been discussed. Design-C takes the ideal symFET operation to a more practical case on 3D-TI. However, there is a complete loss of resonance in Design-C. Therefore, best results

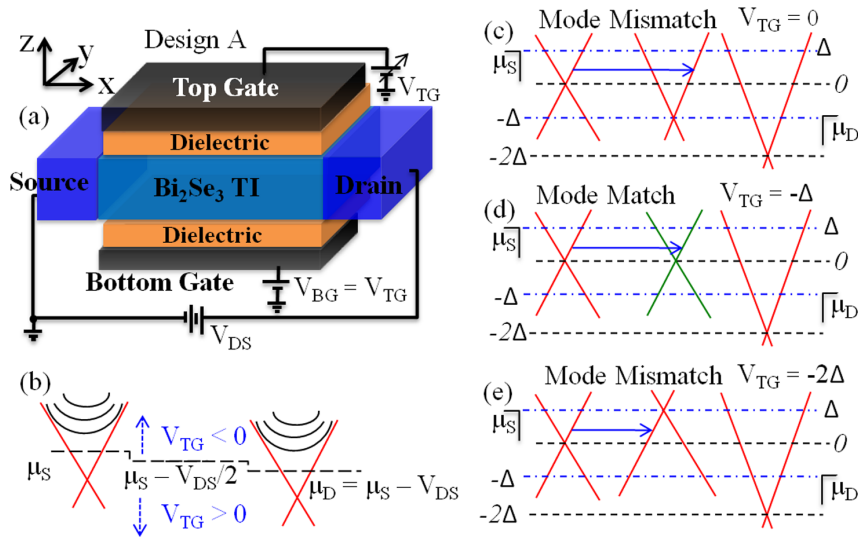


**Figure 1** | (a) Device Structure (Design-A) for quantum transport modeling through  $\text{Bi}_2\text{Se}_3$  slab with shorted top and bottom gates. (b) Potential distribution along the transport direction.  $\mu_{\text{S}}$  and  $\mu_{\text{D}}$  are electrochemical potential at the source and drain end respectively. Gate voltage  $V_{\text{TG}}$  shifts the potential energy in the channel.  $\Delta$  represents the energy difference between  $\mu_{\text{S}}$  and the Dirac-point in the source contact and is used as a reference energy scale throughout this work. (c, d, e) Schematic of the band profile along the transport direction (source, channel and drain from left to right) for three different gate voltages, illustrating the mechanism of mode matching. At 0 K transport is within the energy window delineated with blue dot-dashed line. Blue arrows depict ballistic transport along the transport direction with conserved transverse (along y-axis) momentum. Green bands in (d) emphasize the band-aligned condition between source and channel region.

are obtained for Design-A although the current ratio, between resonance state ( $I_{\text{R}}$ ) and non-resonance state at zero gate voltage ( $I_0$ ), is still relatively small and the device transfer characteristic is sensitive to temperature. Accordingly, suggestions to further improve the ratio for Design-A are provided.

The work is organized as follows. In methods section, the device Hamiltonian is introduced and the methodology for computing transport is explained. Results and Discussion section discusses the results of our simulations and unravels the effect of band-alignment operation on the carrier transport in 3D-TI devices. This is followed with the summary and conclusions of our study. The supplementary material provides the mathematical proofs of some important concepts discussed in this work for more rigorous readers.

## Methods

For describing the device Hamiltonian, the parameters extracted from ab-initio calculations, are optimized for both in-layer and inter-layer coupling to fit the experimentally observed energy-dispersion for  $\text{Bi}_2\text{Se}_3$  as elaborated in our previous work<sup>15</sup>. Each infinite quintuple layer (QL  $\sim 0.943$  nm)<sup>8</sup> (x-y plane; see Fig. 1(a)) of  $\text{Bi}_2\text{Se}_3$  is described by basis set of up and down  $p_z$  orbital of two equivalent Se atoms in k-p model by  $H_{\text{p}}$  as,

$$H_{\text{p}} = \begin{pmatrix} k^2/m_1 & d + k^2/m_2 & ivk_x - vk_y & 0 \\ d + k^2/m_2 & k^2/m_1 & 0 & -ivk_x + vk_y \\ -ivk_x - vk_y & 0 & k^2/m_1 & d + k^2/m_2 \\ 0 & ivk_x + vk_y & d + k^2/m_2 & k^2/m_1 \end{pmatrix}, \quad (1)$$

where  $v = 2.5$  eV-Å is the Fermi velocity,  $m_1 = 0.125$  eV-Å<sup>-2</sup> and  $m_2 = -0.04$  eV-Å<sup>-2</sup> are the orbital masses and the parameter  $d = -0.22$  eV is introduced to generate a gap. The hopping between adjacent layers (z-axis) is described by tight-binding parameter  $t_z = 0.35$  eV in hopping matrix T as,

$$T = \begin{pmatrix} 0 & 0 & 0 & 0 \\ t_z & 0 & 0 & 0 \\ 0 & 0 & 0 & 0 \\ 0 & 0 & t_z & 0 \end{pmatrix}, \quad (2)$$

In the x-direction,  $k_x$  wave-vector in Eq. (1) is discretized by substituting it with  $-i\partial/\partial x$ . Transverse direction (y-axis) is modeled in k-space (eigenmodes) assuming periodic condition (infinite width) because there is no potential variation along y-axis<sup>16</sup>. Non-Equilibrium Green function (NEGF) algorithm<sup>17</sup> with Recursive-Green function<sup>18</sup> is implemented to describe the ballistic transport through a defect-free 3D-TI device. Ideal contacts are modeled as semi-infinite channel region and the contact

self-energy is computed from self-consistent solution of surface green function<sup>19</sup>. The spatial distribution of inhomogeneous potential in the all three devices, because of concurrent application of both gate and channel bias and the potential drop at contact leads, has also been modeled within NEGF formalism. The detailed potential distribution for Design-A and Design-B-C has been elaborated in results and discussion section for lateral and vertical transport, respectively. Next, the gates are phenomenologically modeled with a translation factor of one to regulate the potential in the channel. We note that self-consistent solution of channel potential with a Poisson solver would disturb the perfect band-aligned resonant condition. Since, this would both degrade the results and eclipse the transport concepts which we in particular want to stress upon, the Poisson equation has not been exercised in this work. However, if the device performance is to be examined for practical implementation, the NEGF transport must be solved self-consistently with Poisson to correct the charge induced potential variation in the system.

## Results and Discussion

Transport behaviour in three different band-alignment device designs is expounded in this section. For Design-A, the transport is only in lateral direction which makes it easy to understand the band-alignment concept. It is furthermore supported with derivations in supplementary section S1 and S2 to provide clear insights into the mechanism. Next we delve into more complex S-shape devices for vertical transport to be in-line with a similar symFET<sup>13,20</sup> proposal on graphene. The transport mechanism and limitations have also been discussed for each design.

**Band-Alignment for Lateral Transport.** Figure 1(a) illustrates the device structure for Design-A with 13 QL thickness (z-axis) and 30 nm channel length (x-axis) along with semi-infinite contact on either sides of the channel. The sample thickness has been chosen to be sufficiently large so that inter-surface coupling effects are negligible<sup>21</sup> because the surface wavefunction decays to nearly zero beyond 10 QL<sup>15</sup>. Top and bottom gates are shorted to have uniform influence on all layers of 3D-TI slab. The potential profile along the transport direction is shown in Fig. 1(b) to illustrate the equal drop of bias voltage ( $V_{\text{DS}}$ ) at the source and drain terminals and a flat potential in the channel, which shifts the energy-bands in the channel and drain region by  $-V_{\text{DS}}/2$  and  $-V_{\text{DS}}$  respectively. An important conceptual point to note here is that the energy bands are strictly defined only in the equilibrium condition i.e. in the absence of channel bias. However, in non-equilibrium, under-

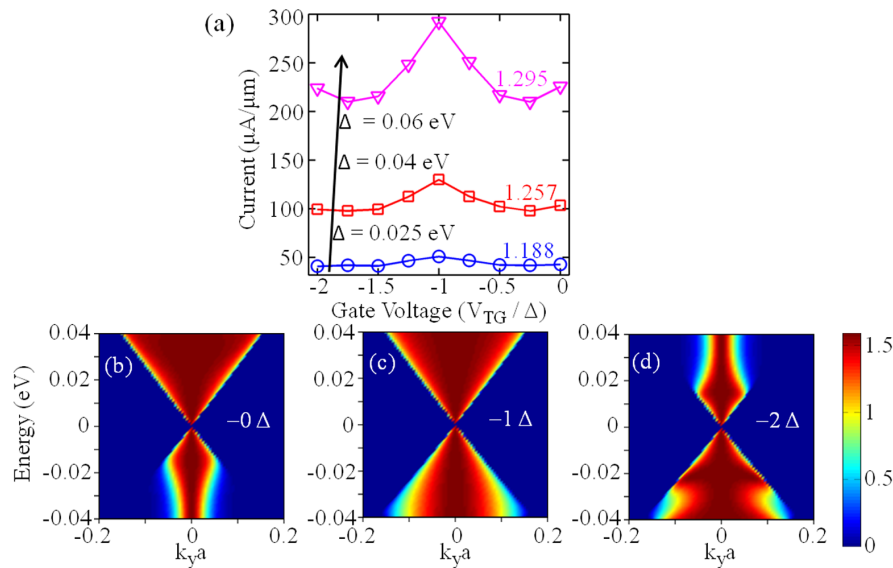


**Figure 2 | Design-A.** (a) Operation for 13 QL thick 3D-TI for three different Fermi-levels in the surface bands ( $V_{\text{DS}} = 2\Delta$ ) at 0 K. Observe the resonant peak at  $-\Delta$ .  $I_{\text{R}}/I_0$  ratio is defined between  $V_{\text{TG}} = 0$  ( $I_0$ ) and  $V_{\text{TG}} = -\Delta$  ( $I_{\text{R}}$ ) and stated over each trendline with respective color. (b-d) Transmission spectrum (in per  $\mu\text{m}$ ) for  $V_{\text{TG}}$  equal to 0 (b),  $-\Delta$  (c) and  $-2\Delta$  (d) at 0 K for  $\Delta = 0.04$  eV as a representative case from (a).

standing in terms of the shift of energy-bands along the transport direction to follow quasi Fermi-level distribution is a good approximation and provides simple insights into transport behaviour (see M. Lundstrom, Fundamentals of Carrier Transport: Cambridge University Press, 2009). Next, also note that because of selenide vacancies<sup>22</sup> a typical sample of  $\text{Bi}_2\text{Se}_3$  TI is n-doped and a small bias applied to electrically characterize the material for ballistic transport should approximately follow potential distribution of Fig. 1(b). Application of gate voltage over such a system would result in a commonly observed ambipolar V-shaped transfer characteristics<sup>23</sup> which are just a signature of Dirac-bands. However, despite of similar device geometry the band-alignment device operates differently as shown in this work.

To assay the transfer characteristics of band-alignment device, a channel bias of  $V_{\text{DS}} = 2\Delta$  (see Fig. 1) has been applied across the device, where  $\Delta$  represents the energy difference between  $\mu_{\text{S}}$  and the Dirac-point in source contact and is used as a reference energy scale throughout this work. Therefore, in equilibrium condition  $\Delta$  equals Fermi-level ( $E_{\text{F}}$ ), with zero-energy level calibrated at the Dirac-point. Energy-bands in the channel are shifted by applying the gate voltage ( $V_{\text{TG}}$ ), which configures it from a purely n-doped ( $V_{\text{TG}} = 0$  volts) to purely p-doped ( $V_{\text{TG}} = -2\Delta$  volts) state (see Fig. 1(c-e)). The resonant condition in this device architecture is achieved at  $V_{\text{TG}} = -\Delta$ , when the bands in the source region are exactly aligned with the bands in the channel so that wavevector modes along both x-axis ( $k_x$ ) and y-axis ( $k_y$ ) are conserved resulting in perfect transmission across the source-channel interface. Also, observe that there is a mode-mismatch across the channel-drain interface, and degrades as the  $V_{\text{TG}}$  is swept from zero to  $-2\Delta$ . This effect manifests clearly in the transport results which we discuss next.

Figure 2(a) illustrates the transfer characteristics of Design-A. It shows a clear evidence of resonant current peaks at  $V_{\text{TG}} = -\Delta$  (see Fig. 1(d)), for different Fermi-levels ( $E_{\text{F}}$ ). For operation in the linear Dirac-bands, the current increases with the increasing magnitude of  $E_{\text{F}}$  because the density of states (DOS) scales linearly with  $E_{\text{F}}$ <sup>24</sup> for Dirac bands, which subsequently increases the current (see Eq. (S1.1)). Furthermore,  $I_{\text{R}}/I_0$  ratio which is defined between  $V_{\text{TG}} = 0$  and  $V_{\text{TG}} = -\Delta$  also increases with the current and becomes more clear at higher  $E_{\text{F}}$ . However, note that since resonance condition requires  $V_{\text{TG}} = -\Delta$  and  $V_{\text{DS}} = 2\Delta$ , further increase in  $E_{\text{F}}$  will drive transport energy range into the bulk bands, while for spintronic

applications we need to operate in the surface-bands to leverage the spin-momentum locking for electrons. This also shows that a new 3D-TI material in future with a larger bulk bandgap may improve the ratio. The transport characteristics are further illustrated via transmission spectrums in Fig. 2(b-d). Specifically notice the band-alignment with nearly symmetric operation about the Dirac-point for  $V_{\text{TG}} = -\Delta$  in Fig. 2(c). Next, since the transverse modes ( $k_y$  modes) for carrier propagation in the device, which is uniform along the y-axis, should always be conserved<sup>25</sup>, the transit from the larger to smaller modes is prohibited and they are filtered out (see Fig. 2 of Ref. 26). Therefore, light bluish-yellow region in Fig. 2(b) and 2(d) show significant mode filtering in valence and conduction band region respectively for  $V_{\text{TG}}$  equal to 0 and  $-2\Delta$ . Mode-filtering also clearly manifests for valence band region in Fig. 2(c) and 2(d) because of the mode-mismatch between channel and drain (see Fig. 1(c-e)). Although, the mode-filtering may seem unlikely for resonance condition in Fig. 2(c), note that unlike graphene, the conduction and valence bands of  $\text{Bi}_2\text{Se}_3$  3D-TI are not symmetric<sup>9,15</sup>. Valence band has smaller Fermi-velocity than conduction band. Therefore, there is mode-filtering in low-energy range even at resonance because electrons attempt to transit from large  $k_y$  modes of valence band in the channel to conduction band in the drain (see Fig. 1(d)) which does not support those modes. There are two additional observations from the transfer characteristics in Fig. 2(a). Firstly, the current at two extremes of  $V_{\text{TG}}$  (0 and  $-2\Delta$ ) is not equal (higher at  $V_{\text{TG}} = 0$ ). Secondly, there is a local minimum on either sides of resonance. The first happens because of mode-mismatch (see supplementary S1) between bands in the channel and drain and therefore is strongest for  $V_{\text{TG}} = -2\Delta$ . The effective DOS in the transport energy window between  $\mu_{\text{S}}$  and  $\mu_{\text{D}}$  (see Fig. 1) is responsible for the second observation, which is mathematically proven in supplementary S2. As the  $V_{\text{TG}}$  is swept from  $-\Delta$  to 0 (or  $-2\Delta$ ), the potential in the channel starts to move the higher DOS out of energy window on one end of the energy-grid and replaces it with lower DOS at another end of the grid, which should have resulted in continuous decrease in current. However, the effect of DOS competes with the mode matching between the source and channel and results in actually higher current at  $V_{\text{TG}} = -\Delta$ . The inflection points mark the transition of dominance of one effect over another.

The effect of temperature on operation of Design-A is next appraised in Fig. 3. The temperature results in the spread of

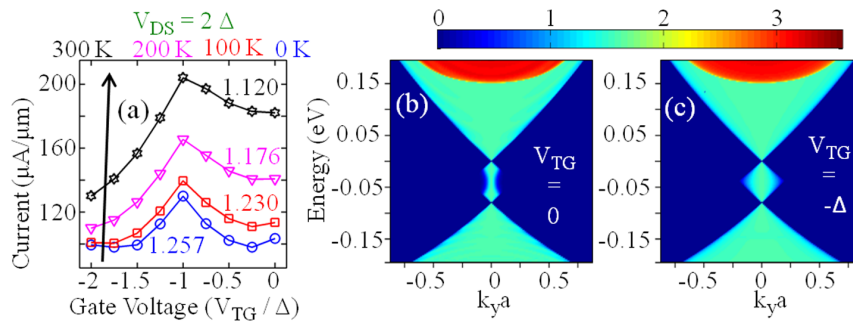


**Figure 3 | Design-A.** (a) Current vs gate voltage at 0 K (blue circles), 100 K (red square), 200 K (magenta triangle) and 300 K (black stars) for  $\Delta = 0.04$  eV.  $I_R/I_0$  ratio and temperature are stated with respective colors for each trendline. Observe that signature of mode matching is severely weakened due to spread in Fermi-distribution. (b, c) Transmission spectrum (in per  $\mu\text{m}$ ) for two gate voltages at 300 K. Compare it with Fig. 2 to observe the extinction of signature of mode match/mismatch in quantum transport. Dark red region is bulk conduction band.

Fermi-distribution and therefore results in the inclusion of wider energy range and  $k_y$  modes for the transport. This results in more number of energy and transverse modes which suffer mode-mismatch either at the source-channel or at the channel-drain interface, mainly the later one, which results in near complete loss of resonance at 300 K as illustrated in Fig. 3(a) by plotting the transfer characteristics and further confirmed via transmission spectrum in Fig. 3(b) and 3(c) respectively for  $V_{TG}$  equal to zero and  $-\Delta$ . In the spectrums, observe that the two zero transmission points (blue dots) at zero  $k_y a$  correspond to the Dirac-points for bands in the source and drain terminal. The resonance condition for  $V_{TG} = -\Delta$  can also be observed by comparing the width of bluish-green region between the two Dirac-points. Furthermore, the bulk conduction band (in red) is more clearly visible than the valence bulk bands (light green-yellow lines) because the Fermi-level is in the conduction band and since the contribution of energy points is weighted by the Fermi-distribution, the transmission is stronger in the bulk conduction band which are nearer to source electro-chemical potential than in the valence bands. Therefore, precisely the averaging of results over more mode-filtered wavevectors wanes the resonance at higher temperatures. Since the  $I_R/I_0$  ratio falls short of values that can be comfortably measured in experiments, for instance around ten<sup>27</sup>, it is important to enhance the ratio. To improve the  $I_R/I_0$  ratio a mode selective switch should be implemented in the channel or at the source-channel interface to completely filter out the non-normal modes ( $k_y \neq 0$ ). This would in general force the device to operate at only one energy point between  $\mu_S$  and  $\mu_D$  at which  $k_y$  would be

conserved, but at resonance condition electrons would be able to conduct at all the energy points because the band-alignment would enable the  $k_y$  conservation at all of the electron energies. This would result in large  $I_R/I_0$  ratio as expected for Graphene symFET in Ref. 13. To achieve the suppression of non-normal modes, tilted gates or an insulating physical barrier like a lens can be implemented in the channel<sup>28</sup>. Heterostructures<sup>29</sup> is another possibility which can be investigated in the future work.

**Band-Alignment for Vertical Transport.** This section investigates two S-shape devices whose architecture is illustrated in Fig. 4(a). The semi-infinite source contact is coupled to 13 bottom QLs (bottom slab), while semi-infinite drain to top 13 QLs (top slab) with 4 QLs in the middle (middle slab). Large thickness of bottom and top slab ensure zero value of surface wavefunction in the middle region. Therefore, for operation solely in the surface bands, electrons must tunnel through the bulk bandgap to transit from source to drain. Next, for Design-B, the top and bottom gate voltages uniformly modulate the doping electronically in respective slabs. For the channel bias  $V_{DS}$ , all layers of bottom (top) slab are hold at  $\mu_S$  ( $\mu_D$ ) electro-chemical potential of the source (drain), while a linear gradient (vertically) is considered in the middle. Note that the physical isolation of layers with contacts on either ends should hold the potential closer to respective contact electrochemical potentials<sup>30,31</sup>, in contrast to Design-A in which both sides of the channel were equally coupled to contacts across all layers and hence had equal drop at both ends (see Fig. 1(b)). Nonetheless, the

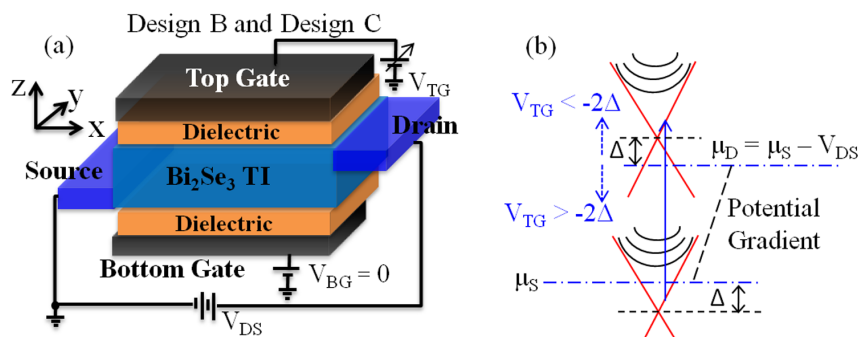


**Figure 4 |** (a) Device Structure for vertical transport in 3D-TI. Source is coupled to bottom few layers (bottom slab) and drain to top few layers (top slab). As a representative case, bottom and top slabs are 13 QL each, whereas middle region is 4 QL. Electrons injected from the source have to tunnel through the middle slab for operation in the bulk band gap. For Design-B, the top and bottom gate voltages uniformly modulate the doping electronically in the respective slabs. For Design-C, a more practical scenario for 3D-TI is presented with uniformly n-doped sample. (b) Potential distribution in x-z plane for band-aligned condition. Blue arrow depicts vertical transport from Dirac-bands of bottom slab to that of top slab, tunneling through the middle region. For channel bias, all layers of bottom (top) slab are hold at  $\mu_S$  ( $\mu_D$ ) electro-chemical potential of source (drain), while a linear gradient is considered in the middle. Gradient for gate potential in Design-B is assumed to be only in the middle region, whereas for Design-C it is from bottom to top layer of the device (across all three regions).



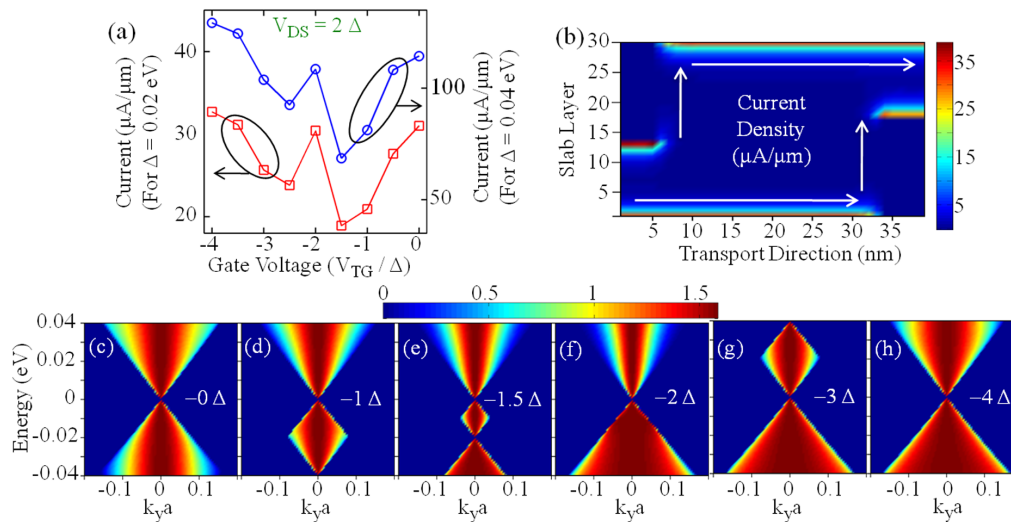


**Figure 5 | Design-B.** (a) Current vs top gate voltage at 0 K for  $\Delta = 0.02$  eV (red squares) and  $\Delta = 0.04$  eV (blue circles). Observe the resonant condition at  $V_{TG} = -2\Delta$ . (b) Illustration of current flow in the device. Observe that the current mainly flows laterally (along x-axis) on top and bottom surface but is forced to transit vertically (z-axis) at the device boundary. (c-h) Transmission spectrum (in per  $\mu\text{m}$ ) for  $V_{TG}$  equal to 0 (a),  $-\Delta$  (b),  $-1.5\Delta$ , (c)  $-2\Delta$  (d),  $-3\Delta$  (e) and  $-4\Delta$  (f) at 0 K for  $\Delta = 0.04$  eV as a representative case from (a).

precise drop at contacts should be computed by solving poisson equation self-consistently which has been explicitly not done as explained in methods section. Gradient for gate potential in Design-B is assumed to be only in the middle region which ensures degeneracy for both the Dirac-bands in source and drain region each. The potential-profile for Design-B warrants that there is absolutely no mode mismatch between bottom (top) layer surface band of source (drain) and bottom (top) slab of the channel. The bottom gate is grounded and top gate voltage is applied to achieve band-alignment condition of resonance which is now expected at  $V_{DS} = 2\Delta$  and  $V_{TG} = -2\Delta$  because potential in top and bottom slab is assumed to be on par with electrochemical potential of the contacts, instead of fifty-percent drop as considered for Design-A. Therefore, for operation of Design-B, doping in the top slab, including drain contact to eliminate mode-mismatch at the top slab-drain interface, is regulated by an electronic equivalent of  $V_{TG}$  value (see Fig. 4(b)). This profile is necessary to emulate the scenario similar to graphene symFET<sup>20</sup> for perfect resonant transmission from the bottom Dirac-band to the top Dirac-band. For Design-C, a more practical scenario for 3D-TI is presented with a uniformly n-doped (de-facto sample) material because experimentally, at least at present to the best of our knowledge, it should be difficult to precisely control the doping to specific layers in 3D-TI. The gate potential gradient is taken from bottom to top layer of device (across all three regions) (see Fig. 4(b)) to follow an expected setup. Such a profile, however introduces mode-mismatch at the top slab-drain interface, as well as, at the top layer of the source contact and the bottom slab. The purpose of having two device designs is to first via Design-B examine the symFET operation comprehensively through quantum transport, to go beyond the analytical evaluation in Refs. 13, 20, and then via Design-C assess its feasibility in 3D-TI because the relaxed and more realistic gate potential gradient in an n-doped sample may deteriorate band-alignment operation.

Figure 5(a) illustrates the transfer characteristics of Design-B. It shows a clear evidence of resonant current peaks at  $V_{TG} = -2\Delta$ , for two different  $\Delta$  values. Since, larger  $\Delta$  also enforces higher Fermi-level for the band-alignment devices discussed in this work, a larger current is observed for  $\Delta = 0.04$  eV (red-squares) than for  $\Delta = 0.02$  eV (blue circles) because higher  $E_f$  also results in transport through energy range with larger DOS (see Eq. (15) of Ref. 24 or Eq. (S2.1)). However, interestingly Fig. 5(a) also illustrates very strong asymmetry about resonant condition, with larger current

for more electronegative gate potentials in strong contrast to Design-A which shows lower current for similar condition. To analyze this anomaly, Fig. 5(b) illustrates the current spectrum in the device. Its ordinate axis represents the QIs of the device (z-axis) while abscissa denotes lateral direction (x-axis). The reddish-yellow color shows the region where current is mainly concentrated in the device while arrows mark the region where most current transits vertically from bottom to top slab. Observe that current flows vertically mainly at the device boundary, otherwise it flows laterally (in-plane) along x-axis. This is in sharp contrast to graphene symFET in which the transport is assumed to be only along the z-axis<sup>13</sup>. In symFET, if the current flow is only along the z-axis, then both  $k_x$  and  $k_y$  wavevectors together constitute the transverse modes (net magnitude equals root of sum of square of both wavevectors), and their conservations acquiesce just one energy point between  $\mu_S$  and  $\mu_D$  for conduction in the non-resonant state and through the entire energy grid for resonant condition resulting in a sharp resonance peak. Since, NEGF quantum transport simulation in Fig. 5(b) shows current flow along x-axis as well, the result implies that only  $k_y$  wavevector must be conserved, analogous to Design-A. A strong resonance peak therefore may not be expected for such a system. Other implications from current distribution in Fig. 5(b) are that firstly the transfer characteristics should strongly be regulated by lateral transport and secondly the vertical tunneling based band-alignment effect may be weaker than initially anticipated. Nevertheless, note that the perfect mode-matching atleast at the contact-channel interface for both the top and bottom slabs simplifies the transport mechanism with respect to Design-A. Furthermore, to advance the understanding of the asymmetry in transfer characteristics, Transmission spectrums for a few  $V_{TG}$  values are illustrated from Fig. 5(c-h) for increasingly negative values. The dark blue spot at 0 eV energy in all spectrums corresponds to the Dirac band for the source contact and the bottom slab, whereas the other dark blue dot for  $k_y = 0$  in Fig. 5(d-h) is consistent with movement of the Dirac-band in the drain contact and the top slab (see Fig. 4(b)). For analyzing these spectrums, recall that valence bands in 3D-TI have lower Fermi-velocity than in conduction bands. Therefore, DOS is higher in valence band region (see Eq. (S2.1)), which results in wider energy-dispersion. For Fig. 5(c), the transport in low energy range is from wider valence band region to more steep conduction band region, which results in mode-filtering (see clipped light blue region in low energy range). All transverse modes are perfectly filtered out at the

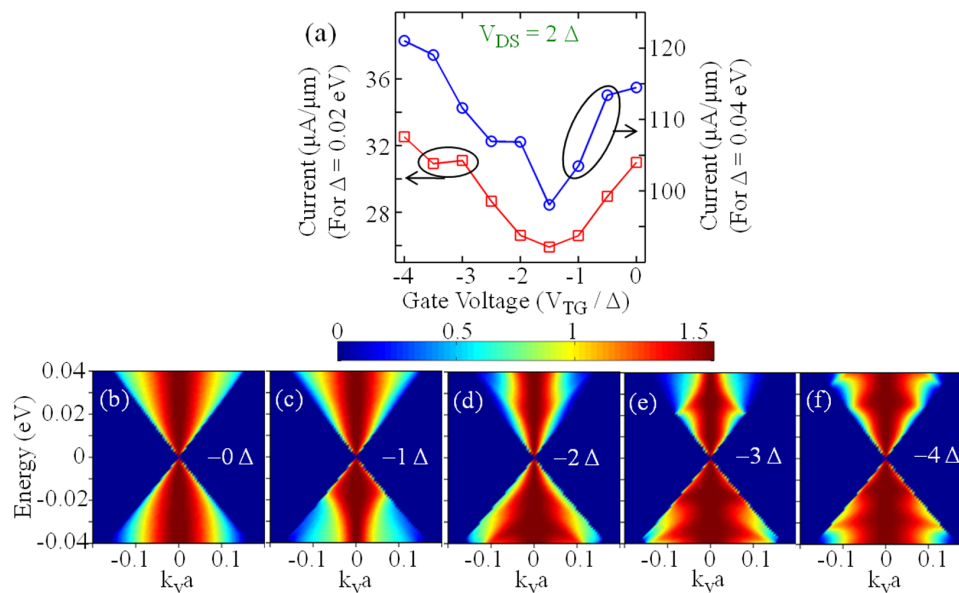


**Figure 6 | Design-C.** (a) Current vs top gate voltage at 0 K for  $\Delta = 0.02$  eV (red squares) and  $\Delta = 0.04$  eV (blue circles). Observe the absence of resonance condition at  $V_{TG} = -2\Delta$ . (b–f) Transmission spectrum (in per  $\mu\text{m}$ ) for  $V_{TG}$  equal to 0 (b),  $-\Delta$  (c),  $-2\Delta$  (d),  $-3\Delta$  (e) and  $-4\Delta$  (f) at 0 K for  $\Delta = 0.04$  eV as a representative case from (a).

energy value corresponding to Dirac-point in the top-slab. Red region in spectrum for  $V_{TG} = -2\Delta$  in Fig. 5(f) shows the band-alignment condition which clearly evinces the largest transmission in comparison to Fig. 5(d), 5(e) and 5(g). However, also recall from the discussion for Design-A and the proof in supplementary S1 that a band-aligned condition results in the lowest DOS configuration in transport energy window. The lateral transport in top layer in high DOS region of conduction band for  $V_{TG} = 0$  and even higher DOS of valence band for  $V_{TG} = -4\Delta$ , results in even higher transmission (see Fig. 5(c) and 5(h)) and current than the resonant condition. Larger DOS in valence bands is also a precursor for the asymmetry observed in Fig. 5(a) (see Eq. (S1.1)). Therefore, although we observe resonant condition in Design-B, the multi-mode conduction and dominance of DOS effect due to lateral transport does not position Design-B as a switch.

Figure 6(a) illustrates the transfer characteristics of Design-C for two different  $\Delta$  values and does not show any resonance behavior. The current is higher for larger  $\Delta$  for the same reason as Design-B above. However, the lowest current point is not at  $V_{TG} = -2\Delta$  as would have been expected for operation in low DOS configuration for the band-aligned condition. The current distribution in Design-C is qualitatively same as illustrated for Design-B in Fig. 5(b); vertical transport is chiefly at the device boundary. Therefore we follow a similar approach to understand these observations, by investigating DOS and mode-matching via Transmission spectrum in Fig. 6(b–f) for increasingly electronegative  $V_{TG}$ . For Fig. 6(b) at  $V_{TG} = 0$ , there is absolutely no difference between Design-B and Design-C, however subsequent application of  $V_{TG}$  in Design-C does not affect the doping in drain contact and it retains same doping as the source terminal. Therefore,  $V_{TG}$  now introduces strong mode-mismatch at the drain-channel interface which degrades further for the larger magnitudes of  $V_{TG}$ , a problem similar to Design-A. Besides, the DOS in the transport energy window and band-alignment for Dirac-bands of the top and bottom slab vie for the effective results. For  $V_{TG} = -\Delta$ , bands in the bottom slab, top slab and drain are positioned similar to Fig. 1(c) for Design-A and therefore Fig. 6(c) shows mode-filtering through yellowish arc in the valence band similar to Fig. 2(b). The surrounding light blue region results from near-perfect lateral transport from the source contact to the bottom slab because there is no mode-mismatch at bottom most layer of the device, although there is a

minor mismatch at top of the bottom slab due to the gate-potential gradient. Next, Fig. 6(d) illustrates the band-alignment condition in Design-C (see Fig. 1(d)). It is this band-alignment operation between the bottom and top slab which results in slightly higher current than  $V_{TG} = -1.5\Delta$  in Fig. 6(a), for an otherwise operation in the lowest DOS configuration (see note for Design-C in supplementary S2). Fig. 6(e) illustrates mode-filtering scenario in Design-C, a case similar to Fig. 1(e) and its corresponding spectrum in Fig. 2(d) of Design-A (compare yellow arc in the conduction band). The light blue region is again due to near-perfect lateral transport in the bottom slab. As  $V_{TG}$  is further increased, the red-region in Fig. 6(f) reveals the high DOS states of valence band and predicts an increase in the current through the device which is observed in Fig. 6(a). Therefore, from transmission spectrum we understand that Design-C inherits few characteristics of both Design-A and Design-B, in which vertical and lateral transport, band-alignment between the top and bottom slab and mode-mismatch at contact-channel interface have to be analyzed simultaneously to understand its transfer characteristics.

Finally, we would like to note that our model indeed shows side surfaces as illustrated in Fig. 1 of our previous work<sup>15</sup>. However, since the thickness of each slab, we consider, is only 13 QL (and additional intermediate slab of only 4 QL for Design-B and C), the strong confinement effect along the z-axis destroys topological side surface states. The previous studies on side-surface for energy-dispersion<sup>32</sup> and transport<sup>33</sup> had considered this axis to be infinite or semi-infinite. Similarly, experimental works to claim evidence of quantum transport through side-surfaces were performed on extremely thick  $\text{Bi}_2\text{Se}_3$  nanowire (140 nm in Ref. 34 and 200 nm in Ref. 35). In fact, if a similar strong confinement were applied along the y-axis, the topological states on the top and bottom surfaces should also be destroyed.

## Conclusion

In summary, this work expatiates on the concept of band-alignment or mode-matching induced resonance to examine the feasibility of a resonant device for  $\text{Bi}_2\text{Se}_3$  3D-TI, a spintronic material. The three different device-designs are evaluated for this purpose. Design-A, which is based only on lateral transport, shows that operation in low DOS energy-range at resonance competes with mode-matching and mode-filtering to manifest the observed transfer characteristics.



It is found that despite of a resonance peak, the  $I_R/I_0$  ratio is not very exciting. The degradation of the ratio is chiefly because the transport in non-resonant condition is not exactly limited to one energy point between contact electro-chemical potentials ( $\mu_S$  and  $\mu_D$ ) as may be expected for Graphene symFET. Therefore, the solutions to limit the transverse modes for improving the device performance have been suggested for future improvements. It is also observed that the rise in temperature degrades the resonance behaviour because of averaging over wider energy and  $k_y$  modes with mode-mismatch. In Design-B and Design-C the vertical and lateral transport, band-alignment between the top and bottom slab and mode-mismatch at contact-channel interface have to be analyzed simultaneously to understand its transfer characteristics. Design-B although exhibits a resonance peak, is found to be less effective than Design-A. Design-C which could be a more realistic implementation on 3D-TI; there is a complete loss of resonance peak. Therefore, as a future direction we suggest to further improve the Design-A design to enhance the ratio for implementing spintronic circuits using 3D-TI.

1. Fu, L., Kane, C. L. & Mele, E. J. Topological insulators in three dimensions. *Phys. Rev. Lett.* **98**, 106803 (2007).
2. Alpichshev, Z. *et al.* STM Imaging of Impurity Resonances on  $\text{Bi}_2\text{Se}_3$ . *Phys. Rev. Lett.* **108**, 206402 (2012).
3. Zhang, X. & Zhang, S. C. Chiral interconnects based on topological insulators. *Micro- and Nanotech. Sens., Sys., and App.* **IV 8373**, 837309 (2012).
4. Akhmerov, A. R., Nilsson, J. & Beenakker, C. W. J. Electrically Detected Interferometry of Majorana Fermions in a Topological Insulator. *Phys. Rev. Lett.* **102** (2009).
5. Hsieh, D. *et al.* A tunable topological insulator in the spin helical Dirac transport regime. *Nature* **460**, 1101–1105 (2009).
6. Pesin, D. & MacDonald, A. H. Spintronics and pseudospintronics in graphene and topological insulators. *Nat. Mater.* **11**, 409–416 (2012).
7. Siu, Z. B., Jalil, M. B. A. & Tan, S. G. Magnetoresistance in Ferromagnetically Coupled Three-Dimensional Topological Insulator Strips. *IEEE Trans. on Mag.* **48**, 4250–4252 (2012).
8. Zhang, H. J. *et al.* Topological insulators in  $\text{Bi}_2\text{Se}_3$ ,  $\text{Bi}_2\text{Te}_3$  and  $\text{Sb}_2\text{Te}_3$  with a single Dirac cone on the surface. *Nat. Phys.* **5**, 438–442 (2009).
9. Xia, Y. *et al.* Observation of a large-gap topological-insulator class with a single Dirac cone on the surface. *Nat. Phys.* **5**, 398–402 (2009).
10. Bala Kumar, S., Jalil, M. B. A. & Tan, S. G. Klein tunneling in graphene systems under the influence of magnetic field. *J. Appl. Phys.* **114**, 084314 (2013).
11. Wu, Z., Peeters, F. M. & Chang, K. Spin and momentum filtering of electrons on the surface of a topological insulator. *Appl. Phys. Lett.* **98**, 162101 (2011).
12. Zhang, L. B., Kai, C., Xie, X. C., Buhmann, H. & Molenkamp, L. W. Quantum tunneling through planar p–n junctions in HgTe quantum wells. *New J. Phys.* **12**, 083058 (2010).
13. Pei, Z., Feenstra, R. M., Gong, G. & Jena, D. SymFET: A Proposed Symmetric Graphene Tunneling Field-Effect Transistor. *Electron Devices* **60**, 951–957 (2013).
14. Atulasimha, J. & Bandyopadhyay, S. Hybrid spintronic/straintronics: A super energy efficient computing scheme based on interacting multiferroic nanomagnets. *12th IEEE Conf. on Nanotech.* (2012).
15. Gupta, G., Lin, H., Bansil, A., Jalil, M. B. A. & Liang, G. Role of acoustic phonons in  $\text{Bi}_2\text{Se}_3$  topological insulator slabs: A quantum transport investigation. *Phys. Rev. B* **89**, 245419 (2014).
16. Venugopal, R., Ren, Z., Datta, S., Lundstrom, M. S. & Jovanovic, D. Simulating quantum transport in nanoscale transistors: Real versus mode-space approaches. *J. Appl. Phys.* **92**, 3730–3739 (2002).
17. Datta, S. *Lessons from Nanoelectronics: A New Perspective on Transport*. (World Scientific Publishing Company Incorporated, Singapore, 2012).
18. Anantram, M. P., Lundstrom, M. S. & Nikonov, D. E. Modeling of nanoscale devices. *P IEEE* **96**, 1511–1550 (2008).
19. Sancho, M. P. L., Sancho, J. M. L. & Rubio, J. Quick Iterative Scheme for the Calculation of Transfer-Matrices - Application to  $\text{Mo}(100)$ . *J. Phys. F. Met. Phys.* **14**, 1205–1215 (1984).
20. Feenstra, R. M., Jena, D. & Gu, G. Single-particle tunneling in doped graphene-insulator-graphene junctions. *J. Appl. Phys.* **111**, 043711 (2012).
21. Kim, D. *et al.* Surface conduction of topological Dirac electrons in bulk insulating  $\text{Bi}_2\text{Se}_3$ . *Nat. Phys.* **8**, 458–462 (2012).
22. Checkelsky, J. G., Hor, Y. S., Cava, R. J. & Ong, N. P. Bulk Band Gap and Surface State Conduction Observed in Voltage-Tuned Crystals of the Topological Insulator  $\text{Bi}_2\text{Se}_3$ . *Phys. Rev. Lett.* **106**, 196801 (2011).
23. Kong, D. *et al.* Ambipolar field effect in the ternary topological insulator  $(\text{Bi}_{1-x}\text{Sb}_x)_2\text{Te}_3$  by composition tuning. *Nat. Nano.* **6**, 705–709 (2011).
24. Castro Neto, A. H., Guinea, F., Peres, N. M. R., Novoselov, K. S. & Geim, A. K. The electronic properties of graphene. *Rev. Mod. Phys.* **81**, 109–162 (2009).
25. Cheianov, V. V., Fal'ko, V. & Altshuler, B. L. The focusing of electron flow and a Veselago lens in graphene p–n junctions. *Science* **315**, 1252–1255 (2007).
26. Sajjad, R. N. & Ghosh, A. W. High efficiency switching using graphene based electron “optics”. *Appl. Phys. Lett.* **99**, 123101 (2011).
27. Masao, N., Hiroki, H., Hiroyuki, K. & Hiroshi, Y. Graphene-Based Nano-Electro-Mechanical Switch with High On/Off Ratio. *Appl. Phys. Express* **6**, 055101 (2013).
28. Gupta, G., Jalil, M. B., Yu, B. & Liang, G. C. Performance evaluation of electro-optic effect based graphene transistors. *Nanoscale* **4**, 6365–6373 (2012).
29. Britnell, L. *et al.* Field-Effect Tunneling Transistor Based on Vertical Graphene Heterostructures. *Science* **335**, 947–950 (2012).
30. Liang, G. C., Ghosh, A. W., Paulsson, M. & Datta, S. Electrostatic potential profiles of molecular conductors. *Phys. Rev. B* **69**, 115302 (2004).
31. Liang, G. C. & Ghosh, A. W. Identifying Contact Effects in Electronic Conduction through C60 on Silicon. *Phys. Rev. Lett.* **95**, 076403 (2005).
32. Moon, C.-Y., Han, J., Lee, H. & Choi, H. J. Low-velocity anisotropic Dirac fermions on the side surface of topological insulators. *Phys. Rev. B* **84**, 195425 (2011).
33. Chu, R.-L., Shi, J. & Shen, S.-Q. Surface edge state and half-quantized Hall conductance in topological insulators. *Phys. Rev. B* **84**, 085312 (2011).
34. Yan, Y. *et al.* High-Mobility  $\text{Bi}_2\text{Se}_3$  Nanoplates Manifesting Quantum Oscillations of Surface States in the Sidewalls. *Sci. Rep.* **4**, 3817 (2014).
35. He, H. T. *et al.* Disorder-induced linear magnetoresistance in (221) topological insulator  $\text{Bi}_2\text{Se}_3$  films. *Appl. Phys. Lett.* **103**, 031606 (2013).

## Acknowledgments

The work at the National University of Singapore was supported by MOE under Grant No. R263000689112 and MOE2013-T2-2-125. Computations were performed on the Cluster at Computational Nanoelectronics and Nanodevices Lab at NUS. M.B.A.J. acknowledges the Singapore National Research Foundation for support under NRF-CRP9-2011-01.

## Author contributions

G.G. and G.L. designed the device structures. G.G. performed the computations and wrote the manuscript. G.G., M.B.A.J. and G.L. critically analyzed the data. All authors reviewed the manuscript. G.L. also managed the overall execution of the project.

## Additional information

**Supplementary information** accompanies this paper at <http://www.nature.com/scientificreports>

**Competing financial interests:** The authors declare no competing financial interests.

**How to cite this article:** Gupta, G., Jalil, M.B.A. & Liang, G. Effect of Band-Alignment Operation on Carrier Transport in  $\text{Bi}_2\text{Se}_3$  Topological Insulator. *Sci. Rep.* **4**, 6220; DOI:10.1038/srep06220 (2014).



This work is licensed under a Creative Commons Attribution-NonCommercial-ShareAlike 4.0 International License. The images or other third party material in this article are included in the article's Creative Commons license, unless indicated otherwise in the credit line; if the material is not included under the Creative Commons license, users will need to obtain permission from the license holder in order to reproduce the material. To view a copy of this license, visit <http://creativecommons.org/licenses/by-nc-sa/4.0/>